Accurate Modeling of Dark-Field Scattering Spectra of Plasmonic Nanostructures

Liyong Jiang,[†,‡,¶] Tingting Yin,[‡,¶] Zhaogang Dong,[§,¶] Mingyi Liao,[∥] Shawn J. Tan,[§] Xiao Ming Goh,[§] David Allioux,[∥] Hailong Hu,[∥] Xiangyin Li,[†] Joel K. W. Yang,[*,§,⊥] and Zexiang Shen[*,‡,∥]

[†]Nanophotonic Laboratory, Department of Physics, Nanjing University of Science and Technology, Nanjing 210094, China, [‡]Centre for Disruptive Photonic Technologies, School of Physical and Mathematical Sciences, Nanyang Technological University, 21 Nanyang Link, Singapore 637371, [§]Institute of Materials Research and Engineering, A*STAR (Agency for Science, Technology and Research), 3 Research Link, Singapore 117602, [∥]School of Physical and Mathematical Sciences, Nanyang Technological University, 21 Nanyang Link, Singapore 637371, and [⊥]Singapore University of Technology and Design, 8 Somapah Road, Singapore 487372. [¶]L.J., T.Y., and Z.D. contributed equally to this work.

ABSTRACT Dark-field microscopy is a widely used tool for measuring the optical resonance of plasmonic nanostructures. However, current numerical methods for simulating the dark-field scattering spectra were carried out with plane wave illumination either at normal incidence or at an oblique angle from one direction. In actual experiments, light is focused onto the sample through an annular ring within a range of glancing angles. In this paper, we present a theoretical model capable of accurately simulating the dark-field light source with an annular ring. Simulations correctly reproduce a counterintuitive blue shift in the scattering spectra from gold nanodisks with a diameter beyond 140 nm. We believe that our proposed simulation method can be potentially applied as a general tool capable of simulating the dark-field scattering spectra of plasmonic nanostructures as well as other dielectric nanostructures with sizes beyond the quasi-static limit.

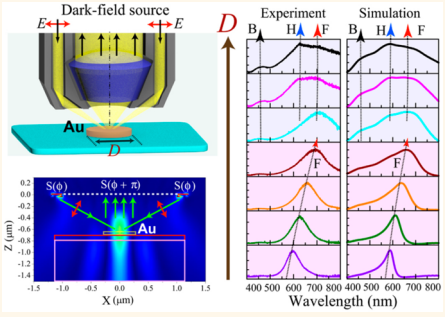

KEYWORDS: dark-field scattering spectra · gold nanodisks · retardation effects · localized surface plasmon resonance · quasi-static limit

Localized surface plasmon resonances (LSPRs)[1−3] on metallic nanostructures have enabled the optical field enhancement in sub-diffraction-limited volume that leads to a host of intriguing applications.[4−8] Over the past few decades, simple metallic nanostructures with various shapes,[9,10] as well as coupled metallic nanostructures, such as dimers,[11−13] trimers,[14,15] nanoshells,[16] nanomatryushkas,[17,18] clusters,[19,20] and nanostars,[21] have demonstrated optical characteristics arising from the fundamental, higher-order, and complex coupled optical states of LSPR.[17,22−24] Current techniques for characterizing their optical properties consist of dark-field scattering,[10,12,15,16,19] photoluminescence (PL),[12,18,21] electron energy-loss spectroscopy,[14,25] two-photon-induced plasmon emission spectra,[26] and scanning near-field optical microscopy.[27,28] Among these techniques, the dark-field scattering spectrum (DFSS) is arguably the simplest approach, with its capability to measure the purely scattered optical states of LSPR for individual metallic nanostructures.

Essentially, DFSS, in either reflection or transmission mode, is measured under the oblique incidence condition with an annular light source. However, an accurate model capable of simulating DFSS has not been thoroughly investigated. For example, current numerical methods for simulating DFSS are normally carried out with the uniform plane wave illumination with either normal or oblique incidence condition from one direction,[20,29,30] where these numerical methods will have the following limitations. First, simulations under the normal incidence condition are usually applied for plasmonic nanostructures with sizes below the quasi-static limit,[1,2] and significant deviations between DFSS experiments and simulations might be observed for plasmonic nanostructures with sizes beyond the quasi-static limit.[29] Such deviations are due to the retardation effects,[31] which will become more pronounced for those relatively

* Address correspondence to zexiang@ntu.edu.sg, joel_yang@sutd.edu.sg.

Received for review June 15, 2015 and accepted September 7, 2015.

Published online September 07, 2015
10.1021/acsnano.5b03622

large nanostructures when using an objective lens with a high numerical aperture (NA).[32] Furthermore, although simulations with plane wave illumination under oblique incidence conditions are able to consider the retardation effects, obvious deviations between experiments and simulations would still appear when studying the size-dependent DFSS of plasmonic nanostructures. This deviation is due to the incident angle used in conventional simulations under oblique incidence conditions that is usually fixed at one specific value, while the real incident angle near the focal plane of the DF light source is varied within a certain range. These limitations make the experimental DFSS for nanostructures with sizes beyond the quasi-static limit lack reasonable microscopical explanations. Therefore, a development of an accurate model for simulating DFSS is in demand from the application point of view.

In this paper, we present a simulation approach that constructs an *annular* light source to closely match the DF light source used in DFSS measurements. This approach was then used to analyze the optical characteristics of gold nanodisks with diameters ranging from 80 to 200 nm, which is beyond the quasi-static limit. The simulation results of DFSS based on our approach agree well with the experimental observations. In comparison, if the simulations were carried out by using the conventional approach with plane wave illumination under either the normal or oblique incidence conditions, significant deviations with respect to the experimental results were observed. We believe that our simulation method could be potentially applied as a general tool capable of acquiring accurate DFSS from both metallic and dielectric nanostructures with sizes beyond the quasi-static limit.

RESULTS AND DISCUSSION

We consider a typical reflection-mode DF scattering system, as illustrated in Figure 1a. Experimentally, the incident white light is focused onto the sample surface through a condenser lens with an annular aperture, where the backscattered light is collected by an objective lens in a confocal setup. We would like to mention that the annular aperture's size in experiment is much larger than incident wavelengths, and the DF beam is different from the typical Bessel optical beams.[33] The working distance of the confocal system is denoted as f_0. The outer and inner NA of the condenser lens is NA_{outer} and NA_{inner}, respectively. The NA for the collection objective lens is denoted as NA_{col}. Figure 1b shows the polarization characteristics of the optical beam as focused on the sample surface through a condenser lens with an annular aperture. It shows that when the linearly *x*-polarized light is passing through the condenser lens, the focused light will be divided into p- and s-polarized beams at oblique incidence with respect to the $x-z$ and $y-z$ planes, respectively. In order to simulate the real DF scattering system, a DF light source was constructed by using two confocal Gaussian beams with designed spot sizes (*i.e.*, D_{outer} = 2400 nm and D_{inner} = 1952 nm) and different NA. In addition, these two optical beams also have a phase shift of π. In the overlapping region, these two beams will experience a destructive interference (see Figure S1 in the Supporting Information). As a result, an annular light source (*i.e.*, the DF light source) will be constructed. Moreover, in our simulation, we mimic the annular light source by using two superposed Gaussian beams, where the electric fields are partially truncated at the square boundary. Although the truncation may bring slight deviations in generating an ideal circular annular light source, such a truncation error is still acceptable for the purpose of simulating the DF illumination (see Figure S1c). A power monitor with a finite width is put near the source plane for detecting the backscattered light to simulate a collection objective lens with a particular NA.

As an example, Figure 1c shows the spatial distribution of the free-space Poynting vector in the $x-z$ plane for a DF light source (NA_{outer} = 0.99, NA_{inner} = 0.985, NA_{col} = 0.9) at the wavelength of 532 nm. We observed a clear destructive interference (see Movie S1) in the overlapping area of the two confocal Gaussian beams and a focal spot with a long focal length in the free space (see Movie S2). The focal center is about 620 nm away from the source plane. The zoom-in profile, as shown in Figure 1d, indicates that the estimated full width at half-maximum (fwhm) of the focal spot is about 220 nm. In addition, it clearly shows the variation of Poynting vectors with different incident angles within the range of the focal spot. Moreover, the detailed distributions of absolute amplitude and incident angle of Poynting vector *P* along the *x*-direction on the focal plane are calculated as shown in Figure 1e,f, respectively.

In experiment, gold nanodisks were fabricated on SiO_2/Si substrates through electron-beam lithography (EBL) and lift-off processes (see Methods). Figure 2 presents both the experimental and theoretical investigations on the optical characteristics of the gold nanodisks with the diameter *D* ranging from 80 to 200 nm, as shown in Figure 2a. Figure 2b shows the DF microscopy images of these samples, where the nanodisks with a diameter larger than 80 nm are hard to be distinguished from their colors. Figure 2c presents the measured DFSS of these samples with NA_{col} of 0.9 (100×), and it shows the red shift of the main fundamental peaks (denoted as "F") when *D* is increased from 80 to 140 nm, where this peak looks symmetric with a Lorentzian profile.

When *D* increases further from 160 to 200 nm, the experimental DFSS shows complex responses. First, the entire spectrum gradually broadens and becomes

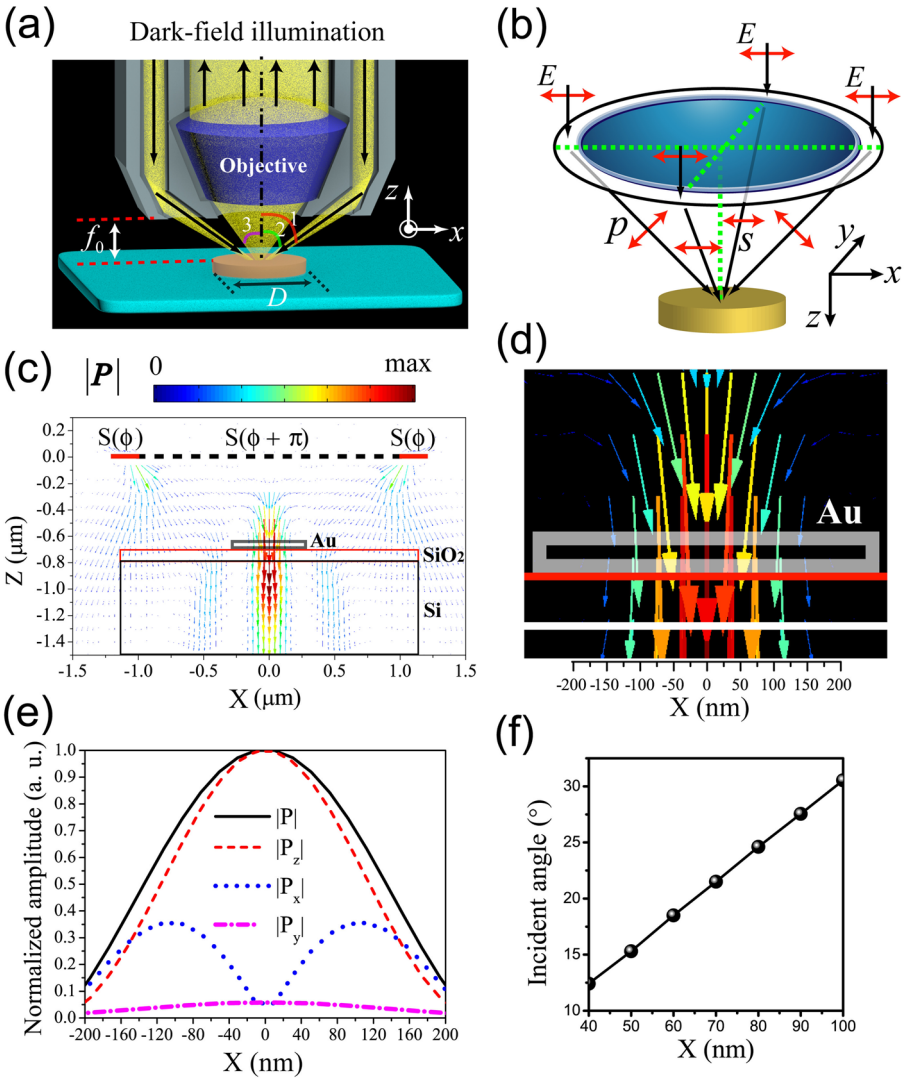

Figure 1. (a) Modeling of a typical reflection-mode DF scattering system. Angles 1 and 2 are the outer and inner incident angles of the DF condenser lens with numerical apertures of NA_{outer} and NA_{inner}, respectively. Angle 3 represents the collection angle of the objective lens. (b) Schematic for the polarization feature of the optical beam as focused onto the sample through a condenser lens with an annular aperture. (c) Simulated distributions of the Poynting vectors in the $x-z$ plane for a DF light source (NA_{outer} = 0.99, NA_{inner} = 0.985) at the wavelength of 532 nm. The linearly x-polarized light is generated by two out-of-phase Gaussian beams, represented by S(ϕ) and S($\phi+\pi$) at z = 0, respectively, and the optical beams are focused onto Au nanodisks on the SiO_2/Si substrate. The backscattered light is collected by a power monitor with a well-defined width. (d) Zoom-in profile of the Poynting vector distributions near the focal plane. (e) Absolute amplitude distributions of the Poynting vector and its components along the x-direction (y = 0, z = −620 nm). (f) Corresponding incident angle distributions of the Poynting vector along the x-direction.

overall blue-shifted. Second, besides the fundamental peak "F", a high-order peak (denoted as "H") and one series of a minor peak (denoted as "B") begin to appear. The peak "B" located at around 450 nm is likely due to the bulk absorption of Au film.[34] Figure 2d presents the corresponding simulated scattering spectra based on the proposed DFSS simulation approach. It shows that the simulated DFSS has a good agreement with the measured one, where the two series of main peaks, "F" and "H", can be clearly observed.

As a comparison, Figure 2e,f presents the simulation results based on the conventional approach of using plane wave illumination at normal incidence and oblique incidence (82°, NA = 0.99) conditions, respectively. There exist significant deviations between simulated and experimental results for those relatively large nanodisks. When light is coming at a normal incidence condition, the main deviation is that no high-order peaks can be observed. For oblique incidence, for either p- or s-polarization, although we can observe both fundamental and high-order peaks, the main deviation is that the overall spectra are always red-shifted.

The high-order peak is due to the retardation-based resonance excited by the horizontal components of incident wave, where a short-range surface plasmon polariton (SPP) mode propagates along the metallic surface and interferes with the reflected SPP to form a

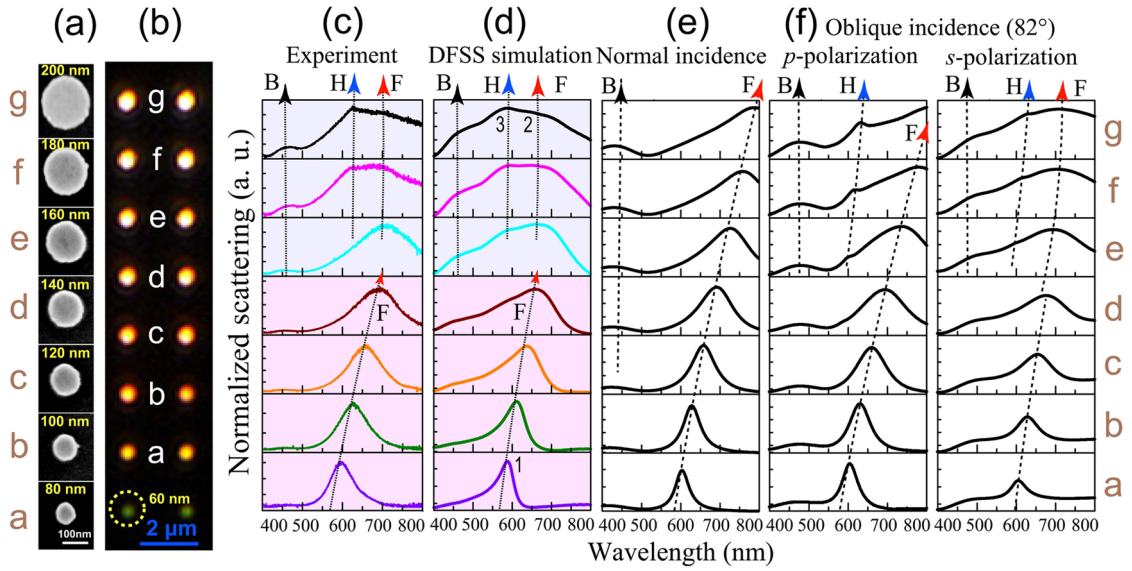

Figure 2. (a,b) Scanning electron microscope (SEM) and DF microscopy images of gold nanodisks with diameters ranging from 80 to 200 nm. The gold nanodisk with a diameter of 60 nm (green) was used as a reference. (c,d) Experimental and simulated DFSS of different gold nanodisks. In both experiment and DFSS simulation, the incident light is polarized along the diameter of gold nanodisks and the collection is unpolarized. The numerical apertures in the DFSS simulation are NA_{outer} = 0.99, NA_{inner} = 0.985, and NA_{col} = 0.9. "F", "H", and "B" denote fundamental, high-order, and bulk absorption peaks, respectively. Simulation results done with plane wave illumination at (e) normal incidence and (f) oblique incidence (82°) conditions.

standing wave in subwavelength metal structures.[35−37] The cavity resonance condition can be written as[36]

$$\frac{2\pi n_{SPP} D}{\lambda_R} = m\pi - \phi \qquad (1)$$

Here, n_{SPP} is the effective refractive index of SPP modes. λ_R is the resonant wavelength. ϕ is the phase shift acquired upon reflection of the SPP at the ends of nanodisk.

The red-shifted behaviors of both fundamental and high-order peaks in simulated results with conventional approaches are well predicted by the theoretical equations. For instance, under the normal incidence condition, the fundamental peak is contributed by the dipolar LSPR along the *x*-direction and its peak position is determined by Mie−Gans extended fomula,[38] which indicates that the resonant wavelength of the LSPR is always red-shifted with an increasing disk diameter (see theoretical equations in Methods). Under the oblique incidence condition, the high-order peak is excited by the horizontal wave vector component. According to eq 1, the resonant wavelength λ_R is proportional to the diameter of gold nanodisks, which accounts for the red-shifted behavior of high-order peaks.

The overall blue shift of the measured DFSS in Figure 2c for those relatively large nanodisks seems counterintuitive as compared to the theoretical results. The reason behind such inconsistency is that the theoretical Mie−Gans formula is applicable under the normal incidence condition, while in practical DFSS measurement, the incident angle at the boundary of the nanodisk is varied gradually with an increasing diameter of the nanodisk (see Figure 1f). Therefore, here we conclude that the overall blue shift is due to the variation of the incident angle at the boundary of gold nanodisks. Our proposed simulation approach can well reproduce the overall blue shift in experiment because it can naturally reproduce the variation of the incident angle at the boundary of gold nanodisks. As a comparison, we did more simulation based on the conventional plane wave illumination approach to show that the blue shift can also be reproduced if we use varying incident angles with disk size (see Figure S2). However, the accuracy of the whole spectra for those relatively large nanodisks is not good enough compared to the experimental data.

In order to gain more insights on the mode profile, which can provide detailed information for the real DFSS scattering process, Figure 3 presents a series of mode analysis for the respective peaks as labeled in Figure 2d. Figure 3a−c shows the Poynting vector distribution (peaks 1 and 3) near the gold nanodisks. We can find a clear backward scattering for the small nanodisk and a strong side scattering for the larger nanodisk. This difference actually reveals the dominated scattering as induced by LSPR and the retardation-based resonance for small and larger nanodisks, respectively. Figure 3d presents the evolution of $|P_z|$ on the top surface of nanodisks, where the boundary component of $|P_z|$ actually represents the backward scattering intensity and the central one denotes the energy of light as focused onto the surface of the nanodisk. As the size of the gold nanodisk increases,

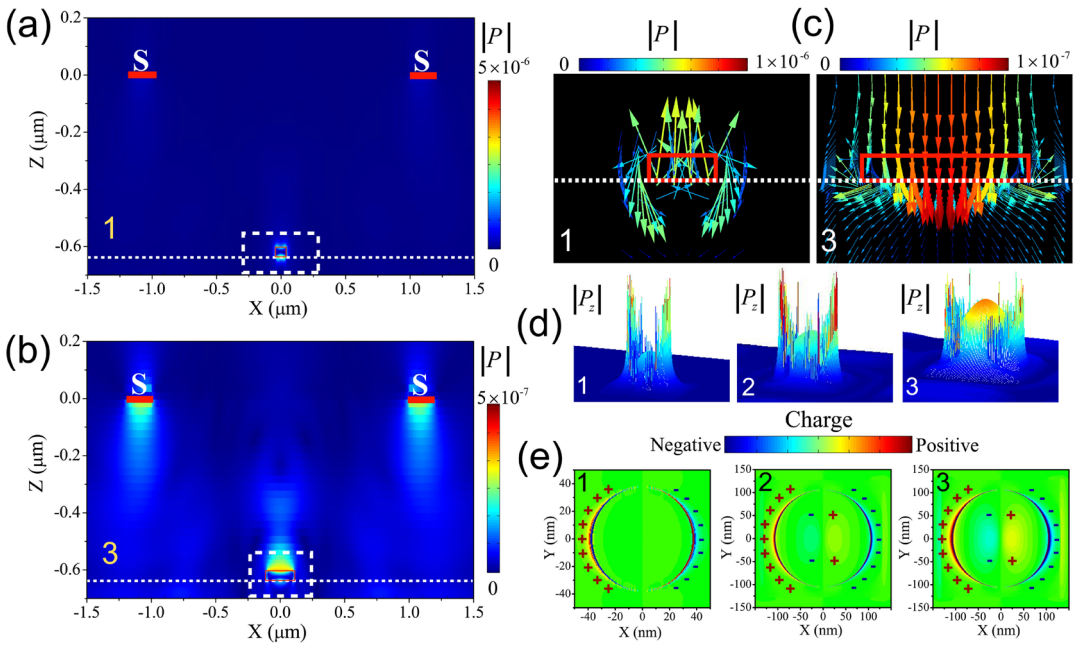

Figure 3. (a,b) Simulated distribution of Poynting vector energy flux $|P|$ in the $x-z$ plane for peaks 1 and 3 in Figure 2d. (c) Poynting vector distribution near the sample as enclosed by a dashed box in (a) and (b). (d) Three-dimensional profile of $|P_z|$ on the top surface of gold nanodisks for selected peaks 1−3 in Figure 2d. (e) Charge density distribution for peaks 1−3.

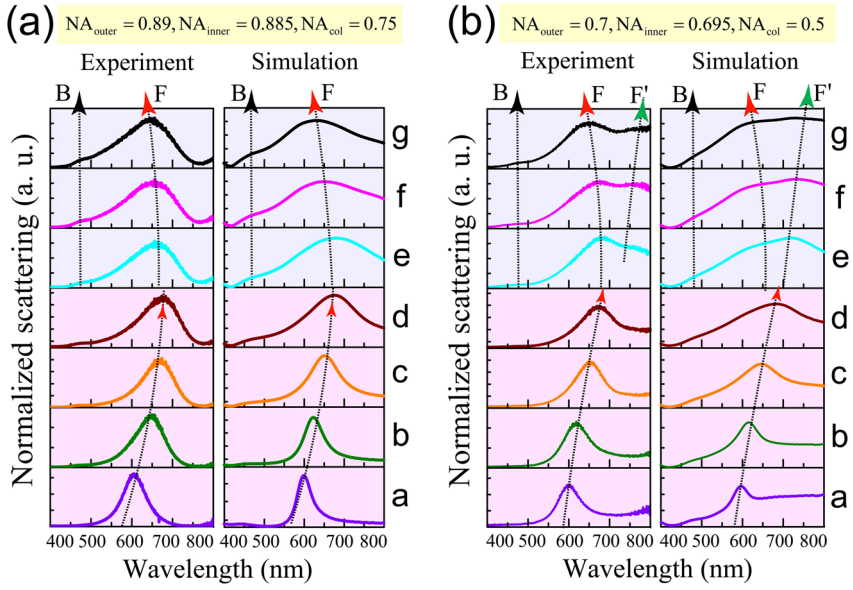

Figure 4. Experimental and simulated DFSS for different gold nanodisks in Figure 2a when different NAs were considered, *i.e.*, (a) $NA_{outer} = 0.89$, $NA_{inner} = 0.885$, $NA_{col} = 0.75$, and (b) $NA_{outer} = 0.7$, $NA_{inner} = 0.695$, $NA_{col} = 0.5$.

the central component will become stronger, and thus it will give rise to enhanced bulk absorption. Moreover, Figure 3e indicates that both fundamental and high-order peaks exhibit a dipolar charge distribution profile on the boundary.

Lastly, we investigated the influence of the NA for the DFSS. First, when $NA_{outer} = 0.89$, $NA_{inner} = 0.885$, and $NA_{col} = 0.75$, only one blue-shifted fundamental peak was observed when D is from 160 to 200 nm, as shown in Figure 4a. The reason behind this response accounts for the degeneration of the retardation effects when the incident angle decreases. In other words, the high-order peak will gradually become degenerate and couple with the fundamental peak to become a single peak. The simulated DFSS matches well with the measured one under $NA_{col} = 0.75$ (100×). Moreover, when NA is decreased further, an additional fundamental peak "F′" can be gradually observed. This additional peak is possibly due to the enhanced contribution from the vertical component of incident wave

(see Figure 2e) with a decreased incident angle. As shown in Figure 4b, the simulated DFSS is able to reproduce the peak response in experimental results with NA_{col} = 0.5 (50×). Furthermore, detailed discussions on the main factors that can influence the DFSS simulation are available in the Supporting Information (see Figure S3).

CONCLUSION

In conclusion, we have presented an approach capable of simulating the DFSS with annular light source at the oblique incidence condition. Based on this simulation approach, we have performed a comprehensive study on the DF scattering properties of individual gold nanodisks. It is shown that the presented DFSS model is able to accurately reproduce the counterintuitive scattering response as the measured one for gold nanodisks with diameters larger than 140 nm, where conventional approaches using plane wave illumination at normal/oblique incidence conditions suffer from the obvious discrepancies between experiments and simulations. The critical advantage of our proposed approach is its ability to reproduce the complex variation of Poynting vector distribution at the boundary of the samples, which accounts for the sensitive scattering of those relatively large samples. The accurate DFSS approach proposed in this work can be widely applied for other noble metal nanostructures and even high-index dielectric nanostructures to predict their unique and complex optical scattering properties.[39]

METHODS

Nanodisk Fabrication. The gold nanodisks were fabricated on SiO_2/Si substrates using EBL and lift-off processes. Silicon was chosen as the substrate to avoid charging effects during the EBL process. The thickness of SiO_2 was 100 nm to reduce the plasmon damping caused by the silicon substrate. Poly(methyl methacrylate) (PMMA) resist (950 K molecular weight, 1.67% in anisole) from MicroChem Corp. was spin-coated at 3k rpm to be ~80 nm on SiO_2/Si substrates. After the spin-coating, the substrates were baked on a hot plate at 180 °C for 120 s. EBL was done with the Elionix ELS-7000 system with an accelerating voltage of 100 keV and a beam current of 100 pA. An optimized exposure dose was used to obtain the structures we designed for the measurements. After exposure, the samples were developed with 1:3 methyl isobutyl ketone/isopropyl alcohol developer at low temperature (−10 °C) for 15 s and then directly blown dry with a steady stream of N_2.[40] Low-temperature development of PMMA provides higher contrast and pattern resolution. Metal deposition was then performed using an electron-beam evaporator (Explorer Coating System, Denton Vacuum). A 30 nm thick gold layer was deposited with a 1 nm thick Cr adhesion layer. The working pressure during the evaporation was below 5×10^{-7} Torr. The temperature of the sample chamber was kept at 20 °C during the entire evaporation process, with the sample holder rotating at a rate of 50 rpm to ensure the uniformity of deposition. Lift-off was done by immersing samples in *N*-methylpyrrolidone solvent at an increased temperature of 65 °C.

Optical Measurements. Dark-field scattering spectra of the gold nanodisks were measured on a confocal Raman microscopy system (WITec CRM200). The scattering spectra were dispersed by a 150 lines/mm grating and detected using a TE-cooled CCD (Andor DV 401-BV-351). A high-resolution spectrograph (0.55 nm/pixel) allows peak positions of scattering to be accurate within ±1 nm. During the dark-field scattering measurement, the sample was illuminated by a halogen lamp (15 V, 150 W, 3150 K) that served as the white source. The light was focused and collected through a Zeiss Epiplan DF objective lens with different NA. To get a good signal/noise ratio, we set the integration time in scattering measurements to 20 s. The final scattering spectra were calculated based on the method in previous work.[12]

Numerical Simulations. Simulation of scattering spectra of gold nanostructures was completed on the software platform FDTD Solutions (Lumerical Solutions, Inc.) based upon the three-dimensional finite-difference time-domain (FDTD) method. The structural parameters of gold nanostructures for modeling were set according to the size measured from SEM images. To get close to real experiments, the SiO_2/Si substrate was considered in the simulation. The Cr adhesion was not included in the simulations for simplification. The complex dielectric constants for gold, SiO_2, and Si were from Johnson−Christy and Palik,[41] respectively. In the dark-field scattering simulations, the dark-field source was constructed by two Gaussian beams with different scale in the $x-y$ plane and a phase difference of π. This will result in a destructive field in the overlapping region of two Gaussian beams. By setting a different virtual NA in the property of Gaussian beams, a confocal dark-field light source can be generated. A power monitor was placed 50−100 nm above the source plane to record the power of backscattered light. The mesh accuracy was set as 6, and an extra fine mesh with a size of 1 nm in the $x-y$ plane and 2 nm along the *z*-direction was added around the gold nanostructures. A perfectly matched layer boundary condition was set for all three dimensions. The Poynting vector energy flux and electric field distributions were obtained from the "frequency domain field and power monitor". The charge distribution was further obtained by calculating the divergence of electric field.

Theoretical Equations. According to Gans's treatment to Mie scattering,[38] the absorption cross section of the nanodisk ($a_1 < a_2 = a_3$) is given by

$$\sigma_{abs} = \frac{2\pi V}{3\lambda}\varepsilon_m{}^{3/2}\sum_{j=1}^{3}\frac{\varepsilon_2/P_j^2}{(\varepsilon_1+(1-P_j)\varepsilon_m/P_j)^2+\varepsilon_2{}^2} \quad (2)$$

$$P_1 = \frac{1+\xi_0{}^2}{\xi_0{}^3}(\xi_0 - \arctan\xi_0) \quad (3)$$

$$\xi_0 = \sqrt{(a_2{}^2/a_1{}^2 - 1)} \quad (4)$$

$$P_2 = P_3 = (1-P_1)/2 \quad (5)$$

where V is the volume of nanoparticle; ε_1 and ε_2 are the real and imaginary dielectric constant of the gold nanoparticle; ε_m is the dielectric constant of the surrounding medium; P_1, P_2, and P_3 are the depolarization factors along the minor (a_1) and major (a_2 and a_3) axes, respectively; ξ_0 is a parameter that depends on the geometry of the nanodisk. Equation 2 indicates that the resonant dipolar LSPR along the a_2 axis occurs when ε_1 is equal to $-(1-P_2)\varepsilon_m/P_2$. Since ε_1 is negative and is inversely proportional to wavelength and $-(1-P_2)\varepsilon_m/P_2$ is proportional to a_2/a_1, an increasing ratio of a_2/a_1 will lead to a red shift of the resonant wavelength for the dipolar LSPR.

Conflict of Interest: The authors declare no competing financial interest.

Supporting Information Available: The Supporting Information is available free of charge on the ACS Publications website at DOI: 10.1021/acsnano.5b03622.

Figures S1−S3 (PDF)

Movie S1: Focusing progress of the DF light source in the $x-y$ plane (MPG)
Movie S2: Focusing progress of the DF light source in the $x-z$ plane (MPG)

Acknowledgment. This work was supported by Singapore Ministry of Education Academic Research Fund Tier 2 (Grant No. MOE2012-T2-2-124) and Tier 3 (Grant No. MOE2011-T3-1-005), the National Natural Science Foundation of China (Grant No. 61205042), and the Natural Science Foundation of Jiangsu Province in China (Grant No. BK20141393). L.Y.J. also would like to acknowledge the financial support from the Zijin Intelligent Program of NUST (Grant No. 2013_zj_010203_16). Z.G.D., S.J.T., X.M.G., and J.K.W.Y. would like to acknowledge the funding support from the Agency for Science, Technology and Research (A*STAR) Young Investigatorship (Grant No. 0926030138), SERC (Grant No. 092154099), and National Research Foundation Singapore (Grant No. NRF-CRP 8-2011-07). L.Y.J. and T.T.Y. greatly acknowledge Prof. N. I. Zheludev for helpful discussions, and Dr. Dongliang Chao and Dr. Guanghui Yuan for useful suggestions.

REFERENCES AND NOTES

1. Kreibig, U.; Vollmer, M. *Optical Properties of Metal Clusters*; Springer-Verlag: Berlin, 1995.
2. Maier, S. A. *Plasmonics: Fundamentals and Applications*; Springer-Verlag: Berlin, 2007.
3. Halas, N. J.; Lal, S.; Chang, W. S.; Link, S.; Nordlander, P. Plasmons in Strongly Coupled Metallic Nanostructures. *Chem. Rev.* **2011**, *111*, 3913–3961.
4. Maier, S. A.; Kik, P. G.; Atwater, H. A.; Meltzer, S.; Harel, E.; Koel, B. E.; Requicha, A. A. G. Local Detection of Electromagnetic Energy Transport Below the Diffraction Limit in Metal Nanoparticle Plasmon Waveguides. *Nat. Mater.* **2003**, *2*, 229–232.
5. Sonnichsen, C.; Reinhard, B. M.; Liphardt, J.; Alivisatos, A. P. A Molecular Ruler Based on Plasmon Coupling of Single Gold and Silver Nanoparticles. *Nat. Biotechnol.* **2005**, *23*, 741–745.
6. Lee, J.; Hernandez, P.; Lee, J.; Govorov, A. O.; Kotov, N. A. Exciton-Plasmon Interactions Inmolecular Spring Assemblies of Nanowires and Wavelength-Based Protein Detection. *Nat. Mater.* **2007**, *6*, 291–295.
7. Kumar, K.; Duan, H. G.; Hegde, R. S.; Koh, S. C. W.; Wei, J. N.; Yang, J. K. W. Printing Colour at the Optical Diffraction Limit. *Nat. Nanotechnol.* **2012**, *7*, 557–561.
8. Huang, Y.-W.; Chen, W. T.; Tsai, W.-Y.; Wu, P. C.; Wang, C.-M.; Sun, G.; Tsai, D. P. Aluminum Plasmonic Multicolor Meta-Hologram. *Nano Lett.* **2015**, *15*, 3122–3127.
9. Kelly, K. L.; Coronado, E.; Zhao, L. L.; Schatz, G. C. The Optical Properties of Metal Nanoparticles: The Influence of Size, Shape, and Dielectric Environment. *J. Phys. Chem. B* **2003**, *107*, 668–677.
10. Mock, J. J.; Barbic, M.; Smith, D. R.; Schultz, D. A.; Schultz, S. Shape Effects in Plasmon Resonance of Individual Colloidal Silver Nanoparticles. *J. Chem. Phys.* **2002**, *116*, 6755–6759.
11. Verellen, N.; Sonnefraud, Y.; Sobhani, H.; Hao, F.; Moshchalkov, V. V.; Van Dorpe, P.; Nordlander, P.; Maier, S. A. Fano Resonances in Individual Coherent Plasmonic Nanocavities. *Nano Lett.* **2009**, *9*, 1663–1667.
12. Hu, H. L.; Duan, H. G.; Yang, J. K. W.; Shen, Z. X. Plasmon-Modulated Photoluminescence of Individual Gold Nanostructures. *ACS Nano* **2012**, *6*, 10147–10155.
13. Slaughter, L. S.; Wu, Y. P.; Willingham, B. A.; Nordlander, P.; Link, S. Effects of Symmetry Breaking and Conductive Contact on the Plasmon Coupling in Gold Nanorod Dimers. *ACS Nano* **2010**, *4*, 4657–4666.
14. Koh, A. L.; Fernandez-Dominguez, A. I.; McComb, D. W.; Maier, S. A.; Yang, J. K. W. High-Resolution Mapping of Electron-Beam-Excited Plasmon Modes in Lithographically Defined Gold Nanostructures. *Nano Lett.* **2011**, *11*, 1323–1330.
15. Mastroianni, A. J.; Claridge, S. A.; Alivisatos, A. P. Pyramidal and Chiral Groupings of Gold Nanocrystals Assembled Using DNA Scaffolds. *J. Am. Chem. Soc.* **2009**, *131*, 8455–8459.
16. Lassiter, J. B.; Aizpurua, J.; Hernandez, L. I.; Brandl, D. W.; Romero, I.; Lal, S.; Hafner, J. H.; Nordlander, P.; Halas, N. J. Close Encounters between Two Nanoshells. *Nano Lett.* **2008**, *8*, 1212–1218.
17. Prodan, E.; Radloff, C.; Halas, N. J.; Nordlander, P. A Hybridization Model for the Plasmon Response of Complex Nanostructures. *Science* **2003**, *302*, 419–422.
18. Ayala-Orozco, C.; Liu, J. G.; Knight, M. W.; Wang, Y. M.; Day, J. K.; Nordlander, P.; Halas, N. J. Fluorescence Enhancement of Molecules inside a Gold Nanomatryoshka. *Nano Lett.* **2014**, *14*, 2926–2933.
19. Fan, J. A.; Wu, C. H.; Bao, K.; Bao, J. M.; Bardhan, R.; Halas, N. J.; Manoharan, V. N.; Nordlander, P.; Shvets, G.; Capasso, F. Self-Assembled Plasmonic Nanoparticle Clusters. *Science* **2010**, *328*, 1135–1138.
20. Lassiter, J. B.; Sobhani, H.; Fan, J. A.; Kundu, J.; Capasso, F.; Nordlander, P.; Halas, N. J. Fano Resonances in Plasmonic Nanoclusters: Geometrical and Chemical Tunability. *Nano Lett.* **2010**, *10*, 3184–3189.
21. Zhang, T. Y.; Lu, G. W.; Shen, H. M.; Shi, K. B.; Jiang, Y. Y.; Xu, D. S.; Gong, Q. H. Photoluminescence of a Single Complex Plasmonic Nanoparticle. *Sci. Rep.* **2014**, *4*, 3867.
22. Rechberger, W.; Hohenau, A.; Leitner, A.; Krenn, J. R.; Lamprecht, B.; Aussenegg, F. R. Optical Properties of Two Interacting Gold Nanoparticles. *Opt. Commun.* **2003**, *220*, 137–141.
23. Nordlander, P.; Oubre, C.; Prodan, E.; Li, K.; Stockman, M. I. Plasmon Hybridizaton in Nanoparticle Dimers. *Nano Lett.* **2004**, *4*, 899–903.
24. Jain, P. K.; El-Sayed, M. A. Plasmonic Coupling in Noble Metal Nanostructures. *Chem. Phys. Lett.* **2010**, *487*, 153–164.
25. Duan, H. G.; Fernandez-Dominguez, A. I.; Bosman, M.; Maier, S. A.; Yang, J. K. W. Nanoplasmonics: Classical Down to the Nanometer Scale. *Nano Lett.* **2012**, *12*, 1683–1689.
26. Wissert, M. D.; Ilin, K. S.; Siegel, M.; Lemmer, U.; Eisler, H. J. Coupled Nanoantenna Plasmon Resonance Spectra from Two-Photon Laser Excitation. *Nano Lett.* **2010**, *10*, 4161–4165.
27. Imura, K.; Ueno, K.; Misawa, H.; Okamoto, H.; McArthur, D.; Hourahine, B.; Papoff, F. Plasmon Modes in Single Gold Nanodiscs. *Opt. Express* **2014**, *22*, 12189–12199.
28. Esteban, R.; Vogelgesang, R.; Dorfmuller, J.; Dmitriev, A.; Rockstuhl, C.; Etrich, C.; Kern, K. Direct near-Field Optical Imaging of Higher Order Plasmonic Resonances. *Nano Lett.* **2008**, *8*, 3155–3159.
29. Knight, M. W.; King, N. S.; Liu, L. F.; Everitt, H. O.; Nordlander, P.; Halas, N. J. Aluminum for Plasmonics. *ACS Nano* **2014**, *8*, 834–840.
30. Knight, M. W.; Fan, J.; Capasso, F.; Halas, N. J. Influence of Excitation and Collection Geometry on the Dark Field Spectra of Individual Plasmonic Nanostructures. *Opt. Express* **2010**, *18*, 2579–2587.
31. Kottmann, J. P.; Martin, O. J. F. Retardation-Induced Plasmon Resonances in Coupled Nanoparticles. *Opt. Lett.* **2001**, *26*, 1096–1098.
32. Fan, J. A.; Bao, K.; Lassiter, J. B.; Bao, J. M.; Halas, N. J.; Nordlander, P.; Capasso, F. Near-Normal Incidence Dark-Field Microscopy: Applications to Nanoplasmonic Spectroscopy. *Nano Lett.* **2012**, *12*, 2817–2821.
33. Yoon, Y.; Li, Q. Y.; Le, V. H.; Jang, W. H.; Wang, T. J.; Kim, B.; Son, S.; Chung, W. K.; Joo, C.; Kim, K. H. Dark-Field Polarization-Sensitive Optical Coherence Tomography. *Opt. Express* **2015**, *23*, 12874–12886.
34. Mooradian, A. Photoluminescence of Metals. *Phys. Rev. Lett.* **1969**, *22*, 185–187.
35. Della Valle, G.; Sondergaard, T.; Bozhevolnyi, S. I. Efficient Suppression of Radiation Damping in Resonant Retardation-Based Plasmonic Structures. *Phys. Rev. B: Condens. Matter Mater. Phys.* **2009**, *79*, 113410.
36. Sondergaard, T.; Bozhevolnyi, S. Slow-Plasmon Resonant Nanostructures: Scattering and Field Enhancements. *Phys. Rev. B: Condens. Matter Mater. Phys.* **2007**, *75*, 073402.

37. Zhu, D.; Dong, Z. G.; Chu, H. S.; Akimov, Y. A.; Yang, J. K. W. Image Dipole Method for the Beaming of Plasmons from Point Sources. *ACS Photonics* **2014**, *1*, 1307–1312.
38. Gans, R. The State of Ultramicroscopic Silver Particles. *Ann. Phys.* **1915**, *47*, 270.
39. Ee, H. S.; Kang, J. H.; Brongersma, M. L.; Seo, M. K. Shape-Dependent Light Scattering Properties of Subwavelength Silicon Nanoblocks. *Nano Lett.* **2015**, *15*, 1759–1765.
40. Yang, J. K. W.; Cord, B.; Duan, H. G.; Berggren, K. K.; Klingfus, J.; Nam, S. W.; Kim, K. B.; Rooks, M. J. Understanding of Hydrogen Silsesquioxane Electron Resist for Sub-5-nm-Half-Pitch Lithography. *J. Vac. Sci. Technol. B* **2009**, *27*, 2622–2627.
41. Johnson, P. B.; Christy, R. W. Optical Constants of the Noble Metals. *Phys. Rev. B* **1972**, *6*, 4370–4379.